

Toward Understanding the Wide Distribution of Time Scales in Negative Bias Temperature Instability

B. Kaczer^a, T. Grasser^b, R. Fernandez^c, and G. Groeseneken^a

^aIMEC, Kapeldreef 75, B 3001 Leuven, Belgium

^bChristian Doppler Laboratory for TCAD at the Institute for Microelectronics,
TU Wien, Gußhausstraße 27–29, A 1040 Wien, Austria

^cUniversitat Autònoma de Barcelona, E 08193 Bellaterra, Spain

Difficulties with evaluating Negative Bias Temperature Instability (NBTI) are linked to fast effects occurring at microsecond or possibly faster time scales. The wide distribution of time scales involved in NBTI relaxation suggests participation of some sort of dispersion in the underlying NBTI mechanism. A universal behavior of the relaxation is observed and used to benchmark several models incorporating dispersion. The impact of the boundary condition on the model based on dispersive transport is also briefly discussed. Furthermore, on-chip circuits are designed and fabricated to measure the effect of AC NBTI up to 2 GHz on individual devices. The results on both single pFET's and inverters indicate that AC NBTI is independent of the frequency in the entire 1 Hz – 2 GHz range. This suggests that any characteristic time scale of the NBTI mechanism must be below 1 ns.

Introduction

The Negative Bias Temperature Instability (NBTI) has recently gained a lot of attention due to its increasingly adverse impact on deep-submicron CMOS technology (1,2). NBTI typically manifests itself by a threshold voltage shift after negative bias has been applied to the pFET gate at elevated temperature (3). The threshold voltage shift is usually determined from I_d - V_g measurements taken during interruption of NBTI stress.

This deceptively simple measurement, however, conceals the complexity of the underlying NBTI mechanism. This is because the effect of NBTI stress starts to recover *immediately* after the gate bias has been removed (4,5). This relaxation has been observed to show approximately logarithmic time dependence and spanning times from at least 10^{-6} to 10^6 s (6-9). This wide range of time scales involved indicates some sort of dispersiveness in the underlying NBTI mechanism. Moreover, it has been noted by several groups that the longer the NBTI stress time, the longer the time needed for the relaxation to reach a given recovery (8,10). Based on this observation we find that the relaxation can be well described by a generalized "universal" relaxation curve (10,11).

Currently, several possible NBTI mechanisms are widely discussed, including hydrogen release from the substrate/gate-oxide interface states and hole trapping in the gate oxide (3,7,12,13). Both hydrogen diffusion and release have been argued as limiting the former effect. Each of these models was extended to include dispersion (13-17). The universal relaxation behavior is used to benchmark these models (11). It is found that none of the present dispersive models fully satisfies this benchmark.

While most of the past work on NBTI has focused on constant (i.e., static or DC) stress, the dynamic (or AC) NBTI data have been sketchy and even contradicting. AC NBTI can be thought of as a fast sequence of stress and recovery phases, with some cut-off frequency presumably indicating a characteristic time of the underlying mechanism. For example, a decrease at and above the kHz and the MHz ranges was hypothesized based on the characteristic times of the interfacial reactions exceeding that of the AC perturbation (5,12).

We have designed on-chip circuits specifically for the purpose of studying the effect of dynamic NBTI stress in the 1 Hz – 1 GHz range, corresponding to times between ~1 ns and 1 s (18). We observe no change in the NBTI shift and hence, no characteristic or “cut-off” time scale of the NBTI mechanism, in this entire range. From a practical perspective, this result should also lead to a simpler, *cumulative* NBTI lifetime extrapolation for a pFET operating during runtime at different frequencies.

NBTI degradation and its recovery

The NBTI V_{th} shift is usually determined during the measurement phase when the gate voltage is lowered to $\sim V_{th}$ to evaluate the V_{th} shift. The (absolute) gate bias is always increased during the stress phase to accelerate the degradation and subsequently decreased to carry out the next V_{th} evaluation. This deceptively simple measurement, however, conceals the complexity of the underlying NBTI mechanism. This main reason for this is the *recovery*, or *relaxation*, of the effect of NBTI stress following *immediately* after the gate stress bias has been removed (4,5). This is illustrated in Fig. 1. Different stress time dependence is obtained depending on the time t_M required to perform each V_{th} measurement.

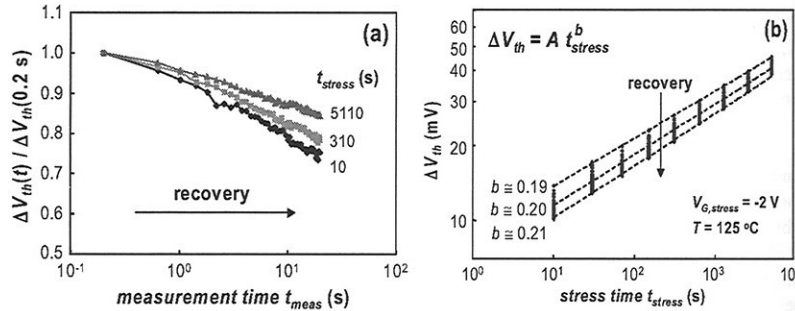


Fig. 1: (a) Considerable recovery of ΔV_{th} is observed upon every interruption of stress during a Measure-Stress-Measure (MSM) sequence (relative recovery for three stress times shown). The exact value of ΔV_{th} thus depends on time t_M elapsed since the beginning of the measurement phase. (b) Recovery of ΔV_{th} as a function of the stress time. Data are fitted for $t_M = \sim 0.2, 5$, and 20 s with $\Delta V_{th} = A t_s^b$. Parameter values A and b clearly depend on t_M .

This relaxation of the NBTI degradation has been observed to show approximately logarithmic time dependence and spanning times from at least 10^{-6} to 10^6 s (6-9). Fig. 2 illustrates the relaxation in the $t_r = \sim 10^{-3}$ to 10^5 range. This wide spread of time scales means that a measurement taking milliseconds to seconds to complete cannot capture the full extent of the degradation.

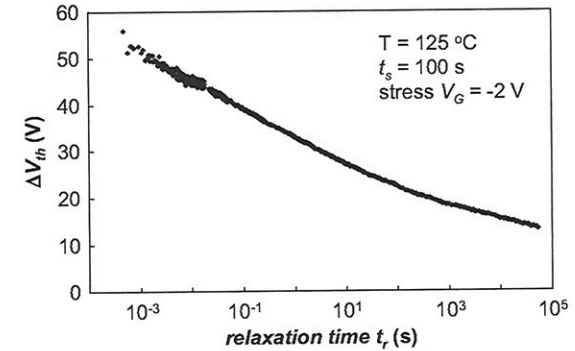


Fig. 2: Relaxation of the NBTI degradation after $t_s = 100 \text{ s}$ stress. The mechanism displays a very long, $\log(t_r)$ -like decay covering 8+ decades.

An alternative evaluation technique, the so-called on-the-fly (OTF) measurement, to study NBTI degradation has recently gained popularity. The technique, illustrated in Fig. 3, infers the amount of degradation directly from the shift of the linear drain current I_D during the stress phase. The corresponding threshold voltage shift can be calculated using (19),

$$\frac{\Delta I_D}{I_D} \approx -\frac{\Delta V_{th}}{V_G - V_{th}}, \quad [1]$$

which assumes I_D degradation due to V_{th} shift only. Alternative OTF technique has been developed (20) to correct the accompanying transconductance degradation (21).

The advantage of the OTF technique lays in completely circumventing any relaxation associated with the finite time needed to switch gate voltage from stress phase to V_{th} measurement (i.e., S→M) during the MSM sequence. However, as has been recently pointed out (22), the problem remains when switching the stress voltage on (i.e., M→S). As suggested in Fig. 3, the shape of the $\log(\Delta I_D)$ - $\log(t_s)$ plot will change dramatically when the current is recorded on a *microsecond* time scale during switching, as opposed to the more typical I_D measurements requiring 10^{-3} to 10^{-1} s (22). This issue casts some doubts on the usefulness of the OTF $\log(\Delta I_D)$ - $\log(t_s)$ plots as a way of projecting the “true” NBTI degradation.

The charge-pumping (CP) technique is sometimes used to evaluate the impact of NBTI degradation on the Si/SiO₂ interface states. During CP, a high-frequency large-amplitude signal is applied to the pFET gate. When the varying gate signal covers voltages spanning both the flat-band voltage V_{FB} and V_{th} , the pFET substrate current can

be measured, which is directly proportional to the interface state density. Disadvantages of this technique include its relative slowness (typically requires at least 0.1 to 10 sec to set up after the stress phase). Far more important, however, is its impact on the outcome of subsequent measurements of NBTI degradation, illustrated in Fig. 4. This issue could be related to the gate voltage V_G crossing the more positive V_{FB} , an intrinsic property of the CP measurement. Application of more positive V_G is known to accelerate NBTI relaxation (8), effectively influencing the subsequent measurement.

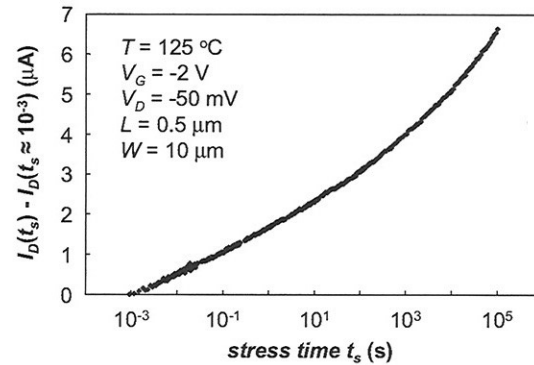


Fig. 3: On-the-fly (OTF) measurement of NBTI degradation. The first current measurement is taken ~ 1 ms after switching V_G to the stress value. The rapid change of I_D at very short stress times indicates the crucial impact of the initial measurement on the final ΔI_D value. This uncertainty in $I_D(t_s=0)$ (i.e., an unknown y-scale offset) will not affect the ΔI_D - $\log(t_s)$ curve shape if the current is plotted on a linear scale, in contrast to the more customary $\log(\Delta I_D)$ - $\log(t_s)$ plot.

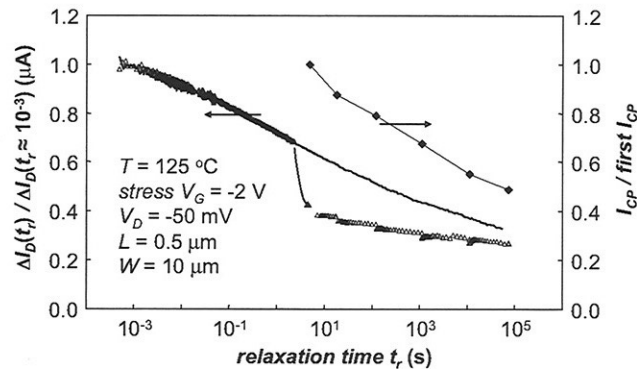


Fig. 4: The long relaxation from Fig. 2 (line) is superimposed on a similar measurement (open triangles), which, however, was interrupted several times by a CP measurement (solid diamonds). A substantial change in the ΔI_D after the first CP measurement is apparent, indicating the invasiveness of the CP technique.

Unfortunately, we have to conclude that no “silver bullet” currently exists to correctly determine and monitor the “true” amount of NBTI degradation. This is chiefly because of the wide distribution of times, stretching down to 10^{-6} , and possibly below, involved in the NBTI mechanism. A successful model for NBTI will have to describe not only the mechanism itself, but will also have to predict how this mechanism will be reflected in various NBTI measurements.

Possible NBTI mechanisms

Currently, two main classes of mechanisms potentially responsible for NBTI are being discussed: hydrogen release, including hydrogen release from the substrate/gate-oxide interface states (3,12) and from semiconductor bulk (23) and hole trapping in the gate oxide (3,7,13). Both hydrogen diffusion and release have been argued as limiting the former effect. NBTI recovery is then understood as either recapture of hydrogen or detrapping of bulk charge.

Provided only a single mechanism is involved in covering the very wide range of times, the OTF measurement, favored by some researchers, appears as the preferred way to study the NBTI stress phase (10). The problem, however, remains with determining the initial current after stress voltage application (22).

It is also possible that NBTI V_{th} shift is in fact a combination of two phenomena: for example, hydrogen recapture responsible for the very long logarithmic relaxation tails (i.e., the slow component; charge trapping in ~ 1 nm SiON films seems unlikely to last up to $10^5 - 10^6$ s), with oxide charge trapping/detrapping “superimposed” at short times (i.e., the fast component) (22). In that case, MSM is a better measure of the dispersive relaxation of the slow component.

Modeling dispersive behavior

Most of the models proposed in the literature can successfully explain the NBTI degradation during the stress phase. However, only a fraction of these models touches upon or attempts to reproduce the very long relaxation tails. We argue that it is this relaxation behavior that can provide important insights into the NBTI mechanism.

The very wide range of time scales involved in relaxation indicates some sort of dispersion in the underlying NBTI mechanism. A dispersive element has been introduced into NBTI modeling by several groups. This included the assumption of dispersive tunneling times (7), dispersive interfacial reaction (16,24), and dispersive, or disorder-controlled transport of hydrogen through the amorphous oxide film (8,12,15,16, 25).

A model introducing dispersion through disorder-controlled transport of hydrogen is depicted in Fig. 5 (8). It is essentially an extension of the Reaction-Diffusion model (12), which assumes classical (Gaussian) hydrogen transport. In this model, hydrogen species is released from the Si-substrate/gate-oxide interface, leaving behind positively charged states with density $N_i(t)$, detected as the threshold voltage shift ΔV_{th} . Some interface states are again repassivated by the released hydrogen. The balance between the hydrogen generation and recombination reactions is controlled by the hydrogen density at

the interface, which in turn is controlled by the diffusion of hydrogen through the oxide. Disorder of amorphous SiO_2 film is introduced into the model by considering localized deep hydrogen states. This results in a very wide distribution, or dispersion of hydrogen hopping times.

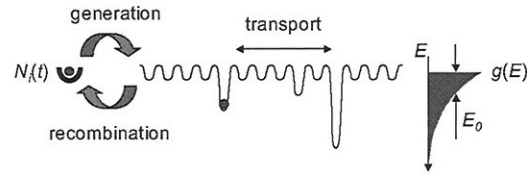


Fig. 5: Schematic of the disorder-controlled kinetics of NBTI. Compared to the classical model, *energy distribution* $g(E)$ of deep localized hydrogen states is assumed in the dispersive case, modifying the transport equation. Diffusing particles spend most of their lifetime in the deep states, which thus control the transport properties.

For exponentially distributed density of localized hydrogen states $g(E)$ and neutral diffusing hydrogen species the model predicts NBTI degradation dependence in the form

$$\Delta V_{th} \propto N_i(t) = A t^b, \quad [2]$$

where the power-law exponent $b = \alpha/2$, α being the so-called *dispersion parameter*

$$\alpha = \frac{k_B T}{E_0}. \quad [3]$$

In Eq. [3], E_0 is the characteristic energy of $g(E)$ (see Fig. 5), k_B the Boltzmann constant and T the temperature. The dispersion parameter α varies between 1 for classical diffusion and approaches 0 for a strongly dispersive system.

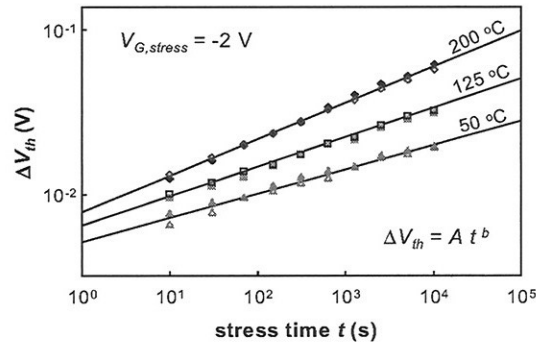


Fig. 6: Shift in pFinFET threshold voltage ΔV_{th} as a function of stress time obtained at 3 different temperatures T (open and closed symbols: two similarly processed wafers). All data can be described by a power-law dependence given in Eq. [2]. It is apparent that the NBTI exponent b (i.e., the slope in the log-log plot) is increasing with increasing T .

In addition to the commonly-observed power-law dependence of NBTI degradation, the dispersive model predicts a linear *temperature dependence of the power-law exponent*. Such a temperature dependence has been observed in MSM measurements (Fig. 6) by several groups (8,13,14,26). The slow MSM measurement captures the behavior of the *slow* states, which are presumably by a dispersive mechanism. In contrast to that, this temperature dependence is not seen in OTF measurements. This could possibly imply that OTF measurements are governed by fast states, which do not show dispersive behavior.

More importantly, the disorder-controlled model predicted the observed $\log(t)$ -like dependence for recovery. The approximate analytical solution has been derived in Ref. (8) as

$$\frac{N(t_r)}{N(t_s)} = \frac{1}{1 + (t_r/t_s)^{\alpha/2}} \quad [4]$$

where t_r is the relaxation time measured from the moment the stress gate voltage has been removed after being applied for time t_s , $N(t_s)$ and $N(t_r)$ are respectively the NBTI shift at the end of stress and during relaxation. This curve behaves logarithmically over many decades around $t_r/t_s \sim 1$ and is physical in asymptotically approaching 1 and 0, at very short and long times, respectively. Introduction of dispersion into the model therefore succeeded in describing the long relaxation tails (Fig. 2).

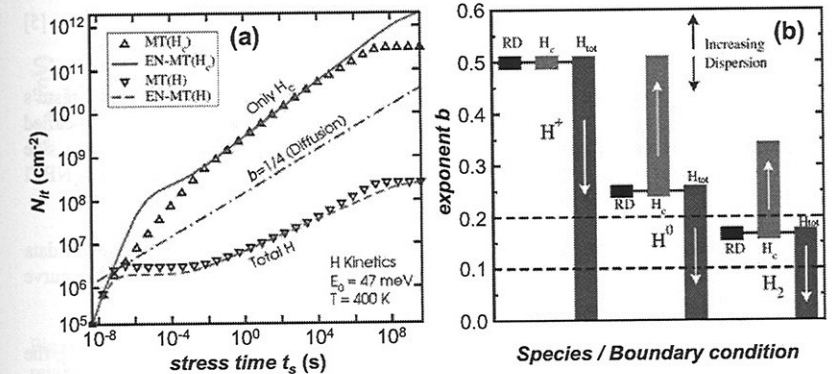


Fig. 7: (a) Increase of interface state density as a function of stress time for the classical case (dash-dotted line), and the dispersive cases with boundary conditions assuming recombination of mobile hydrogen (H_c) only (solid line) and all hydrogen (dashed line). The power-law exponent increases (decreases) for the former (latter) boundary condition. Symbols: numerical simulation (25). (b) Summary of power-law exponent dependence for increasing dispersion in the system for hydrogen ions (H^+), neutral hydrogen (H^0) and hydrogen molecule (H_2) as the transported species. Depending on the boundary condition (only mobile hydrogen " H_c " or all hydrogen " H_{tot} " recombination), the exponent can both increase and decrease.

From Eq. (3) it is apparent that introducing deeper localized hydrogen states (essentially hydrogen “traps”) into the oxide layer results in increased dispersiveness of the system and a *reduced* ΔV_{th} - t power-law exponent. This argument was also used to explain differences between pure SiO₂ and SiON films, the latter being arguably more dispersive due to increased disorder after nitrogen incorporation (27).

On the other hand, it has been shown (28) that the introduction of traps in the oxide would result in an *increase* of the power-law exponent. This contradiction has been traced to the boundary condition at the Si-substrate/oxide interface (25). If only recombination of the mobile (i.e., non-trapped or “conduction-band”) hydrogen at the interface is assumed, the power-law exponent increases with respect to the classical value. If, on the other hand, recombination of *all* (i.e., mobile *and* trapped) hydrogen at the interface is allowed, lower exponents are seen, as is shown in Fig. 7. This latter case appears less physical, it, however, results in a reduction of the power-law exponent at increasing dispersion of the system or at lower T [see Eq. (3)], an effect experimentally observed (Fig. 6).

Universality of NBTI relaxation

The asymptotic relaxation behavior described by Eq. (4) depends on the ratio $\xi = t_r/t_s$ only, i.e., the longer the NBTI stress time t_s , the longer the time needed for the relaxation to reach a given recovery (8,10,11). Based on this observation we find that the relaxation can be well described by a generalized (“universal”) relaxation curve (11)

$$r(\xi) = \frac{N(t_r)}{N(t_s)} = \frac{1}{1 + B\xi^\beta}, \quad [5]$$

where B is a fitting parameter close to unity and β an inverse measure of the mechanism’s dispersiveness. Curiously, the function has many properties similar to the so-called stretched exponential, often invoked to model dispersive phenomena (15). As a side note, the same functional form (with negative β) is used in Ref. (13) to describe the NBTI stress phase.

The universality of relaxation (10,11) is illustrated in Fig. 8. The relaxation data taken after different stress times t_s after rescaling fall on the same universal curve described by Eq. [5].

The universal relaxation behavior has an intriguing implication. Using Eq. [5], the relaxed value of ΔV_{th} measured with delay t_M in a MSM measurement after total stress time t_s can be described as

$$\Delta V_{th}(\xi) = \frac{At_s^b}{1 + B(t_M/t_s)^\beta}. \quad [6]$$

Eq. [6] can be potentially used to correct MSM measurements to zero measurement time t_M (corresponding to zero relaxation, i.e., $t_r = 0$ s) to find the “true” degradation curve (11). This is illustrated in Fig. 9. Note that in both measurements, a significant relaxation is observed up to the longest stress times.

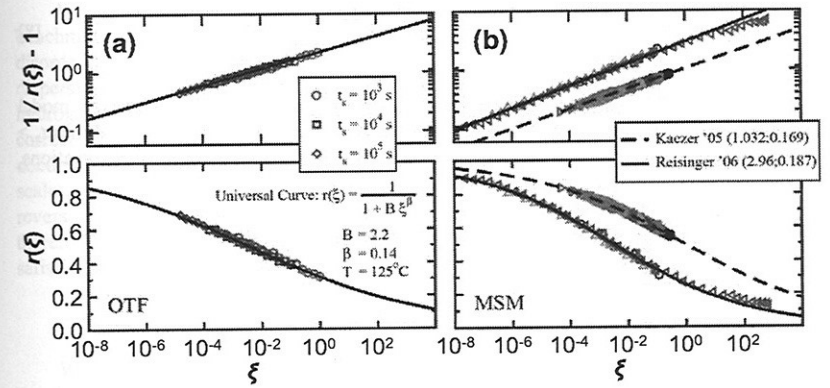


Fig. 8: (a) Demonstration of universal alignment for the OTF data of Ref. (10). The different symbols represent different stress times. The larger the stress time, the further the data moves to the left on the universal curve. Note the linear behavior of $1/r - 1$ on the log-log scale. (b) Additional examples of universal relaxation for the MSM data from Ref. (8) and the fast MSM data from Ref. (9).

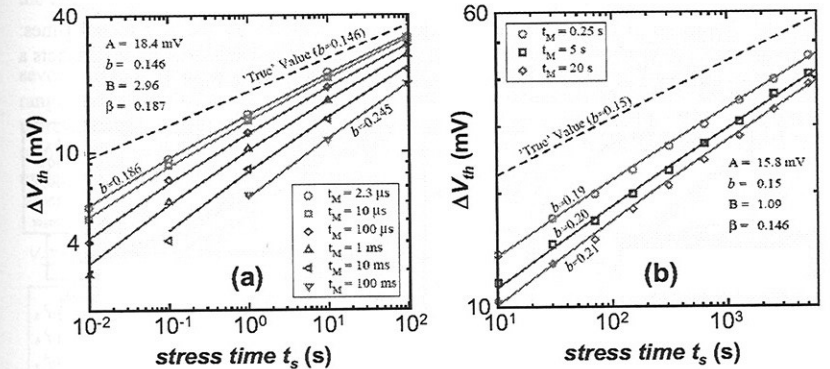


Fig. 9: Comparison of the analytic model for MSM measurements based on the universal relaxation to the data of Ref. (9) (a) and Ref. (8) (b). The “true” NBTI degradation can be recovered fitting Eq. [6] into the MSM data and by extrapolating to $t_M = 0$ s.

In contrast to that, the relaxation curve of the classical Reaction-Diffusion model (12,29), which can be analytically expressed as (cf. Eq. [5]) (11)

$$r(\xi) = \frac{1}{1 + \xi^{1/2}}, \quad [7]$$

results in the corresponding analytic description of delayed MSM ΔV_{th} measurements (cf. Eq. [6])

$$\Delta V_{th}(\xi) = \frac{At_s^b}{1 + (t_M/t_s)^{1/2}} \quad [8]$$

As is shown in Fig. 10, Eq. [8] derived from the classical Reaction-Diffusion model predicts virtually no effect of delayed measurement (i.e., relaxation) for stress times $t_s > \sim 10t_M$. As was already noted in Ref. (22), this is in contradiction with the observations, such as those in Figs. 9 and 1b.

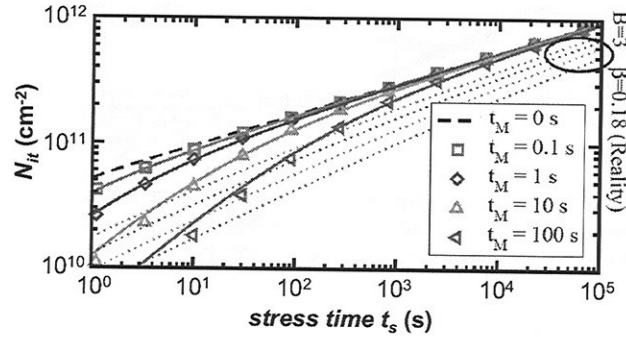


Fig. 10: Influence of the measurement delay t_M as predicted by the RD model (lines: analytic solution, symbols: numerical solution). The Reaction-Diffusion model predicts a very small influence of delay for longer stress times, in contrast to Figs. 1b and 9.

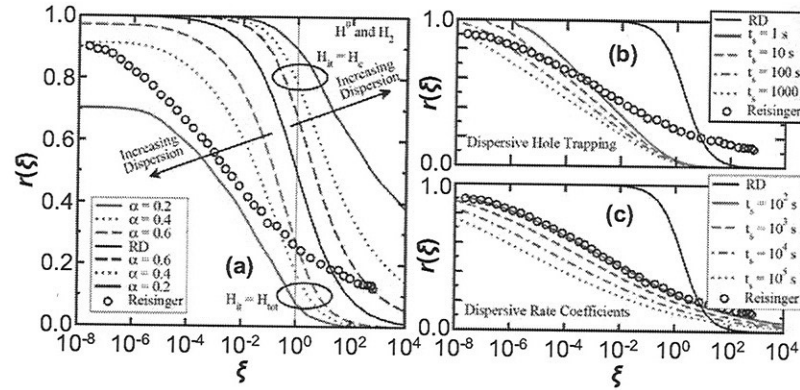


Fig. 11: (a) Relaxation behavior as predicted by the full numerical solution of the disorder-controlled transport models for various values of the dispersion parameter α . Also shown is the data from Ref. (9) as a reference. Depending on the boundary condition, the model always stays below or above the classical Reaction-Diffusion limit. (b) Relaxation as predicted by a simple dispersive hole trapping model [parameters from Ref. (7)]. (c) Relaxation as predicted by a dispersive reverse-rate reaction rate model. The latter two models do not scale universally.

We further propose to use the observed universality of relaxation as an additional benchmark for several existing NBTI models (11), namely i) the above-mentioned disorder-controlled hydrogen transport, ii) the dispersive hole trapping (7), and iii) the dispersive reaction rate (13,17) models. Eq. [4] of our original disorder-controlled hydrogen transport model scales universally, however, introducing apparently more correct physical assumptions can result in non-universal scaling (11). Fig. 11a documents that the refined model is still capable of reproducing the wide range of time scales. The simple dispersive hole trapping model and the model based on a dispersive reverse reaction lack the universal scaling, as can be seen in Fig. 11b and 11c. We therefore have to conclude that none of the current models incorporating dispersion satisfies all required benchmarks.

Dynamic NBTI

While most of the past work on this topic has focused on the static (i.e., DC) stress, the dynamic (i.e., “AC”) NBTI data have been sketchy and even contradicting. Some works have indicated no or weak frequency dependence of AC NBTI (5,12,28), while some reported or discussed an AC NBTI decrease in or toward the MHz range (12,28,30,31). Regarding theoretical predictions, NBTI frequency independence was derived from the original Reaction-Diffusion model (29) for lower frequencies. A decrease at and above the kHz (28) and the MHz (12) ranges was hypothesized based on the characteristic times of the interfacial reactions exceeding that of the AC perturbation.

From a practical perspective, today’s CMOS logic operates at frequencies between several GHz (processor core), 100’s of kHz (L1 and scratchpad caches), down to the kHz range and below (L2 and L3 caches). Consistent data collected on a single sample set are therefore needed over this wide frequency range to allow prediction of NBTI degradation in present and future CMOS technologies, and to provide a basis for better theoretical understanding of the NBTI mechanisms.

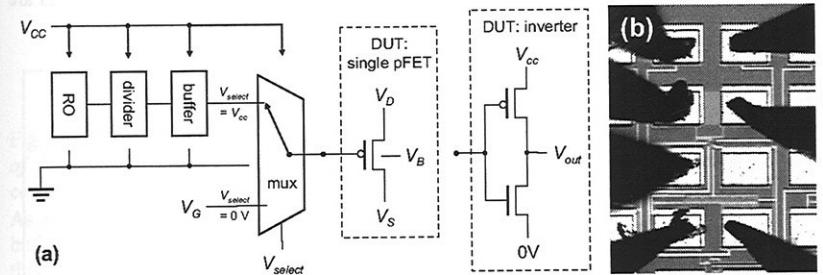


Fig. 12: (a) The circuit for on-chip studies of DC and AC NBTI consists of a 41-stage ring oscillator, a frequency divider, a buffer, a pass-gate-based multiplexer, and the device under test (DUT), which is either a single pMOS or an inverter. When $V_{select} = 0$ V, V_G is connected to the DUT, allowing for direct stressing and characterization. When $V_{select} = V_{cc}$, the DUT is connected to the oscillator, resulting in very high frequency AC stress (duty cycle 50%). $L = 0.13$ μ m, pFET $W = 2$ μ m, inverter $W_p = 6$ μ m, $W_n = 3$ μ m. (b) Micrograph illustrating the fabricated circuit under test.

On-chip circuit description

On standard DC FET test structures, the measurement of AC NBTI effects is limited by the inability to reliably pass large-amplitude AC signals $> \sim 1$ -10 MHz onto the gate of the tested device (due to parasitic effects such as cable capacitance, signal reflection at the device, etc.). Studying the effects of AC NBTI stress on all devices of a ring oscillator is obscured by the indirect extraction of the V_{th} shift and the superposition of additional effects (32). We have therefore designed dedicated on-chip circuits allowing accurate study NBTI AC stress up to the GHz range (18).

The circuit used in our experiment is schematically depicted in Fig. 12. It consists of a ring oscillator, a frequency divider, a buffer (33), a pass-gate-based multiplexer, and the device under test (DUT), which is either a single pMOS or an inverter. Multiple copies of the circuit were drawn on the die with frequency divider ratios 1:1 (no divider) to 1:256, covering the frequencies ~ 7 MHz – 2 GHz. Additionally, copies of the circuit without the ring oscillator branch were drawn, allowing for the DUT's stressing from an external pulse source, covering the 1 Hz – 1 MHz range. The multiplexer is used to select either the direct access to the DUT gate ($V_{select} = 0$ V) or the application of AC signal to the DUT ($V_{select} = V_{cc}$). The circuits were fabricated in the conservative $0.13 \mu\text{m}$ CMOS flow, with SiON gate dielectrics with EOT = 1.4 nm.

Note that the DUT is biased as in a real CMOS circuit, i.e., the DUT is stressed when the input is at 0V. The NBTI stress voltage is selected by the circuit's supply voltage V_{cc} .

Static and dynamic NBTI in 1 Hz – 1 GHz frequency range

A DC NBTI MSM sequence at several stress voltages performed using the on-chip circuit is shown in Fig. 13a. The same stress sequence but with AC NBTI stress at $f = 7.4$ MHz generated on-chip is shown Fig. 13b. It is apparent that the general trend of the AC NBTI stress is identical to the DC NBTI (Fig. 13a); in both cases ΔV_{th} vs. t_{stress} following a power law with identical exponents. Both DC and AC NBTI voltage accelerations are shown to be equivalent in Fig. 14.

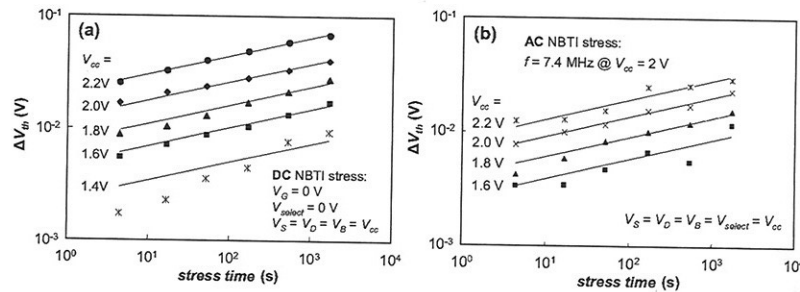


Fig. 13: ΔV_{th} as a function of stress time t_s for varying stress voltage for (a) DC and (b) AC NBTI stress conditions. Both data sets are fitted with a power law with the respective exponents common for all stress voltages. Typically observed exponents are 0.17-0.20.

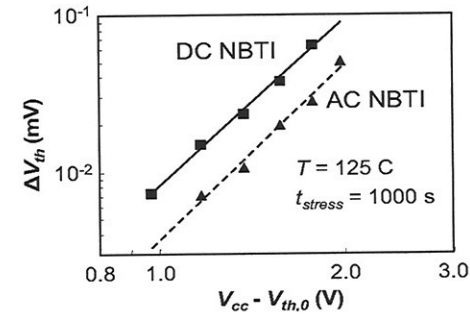


Fig. 14: AC NBTI voltage (i.e., gate oxide field) acceleration is found to be equivalent to the DC NBTI voltage acceleration. AC data were averaged from measurements taken over the entire frequency range.

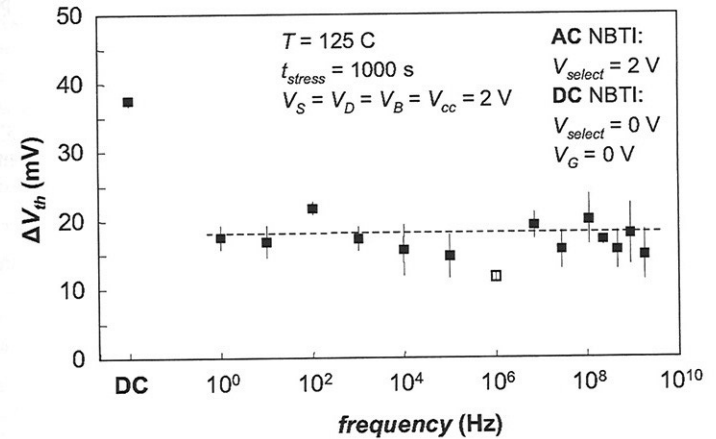


Fig. 15: The V_{th} shifts due to AC NBTI stress in a single pFET are seen to be independent of frequency in the entire frequency range of 1 Hz – 2 GHz. The result of the corresponding DC NBTI stress obtained on identical devices is shown for comparison. As a side note, the low ΔV_{th} shift at 1 MHz (open symbol), taken on a circuit without a buffer, illustrates the caveats of using an external pulse source to study AC NBTI. Were this the highest frequency point, an incorrect conclusion about the AC NBTI frequency dependence could be drawn.

The frequency dependence of the V_{th} shift after 1000 s of AC NBTI stress measured on devices on the same wafer over the entire measured frequency range of 1 Hz – 2 GHz is shown in Fig. 15. For comparison, the DC result is also included. As reported before (5), NBTI V_{th} shifts due to AC stress are $\sim 2\times$ lower than their DC counterpart. However, Fig. 15 extends these results and shows that the NBTI V_{th} shifts due to AC stress are independent of frequency in the wide range of 1 Hz – 2 GHz.

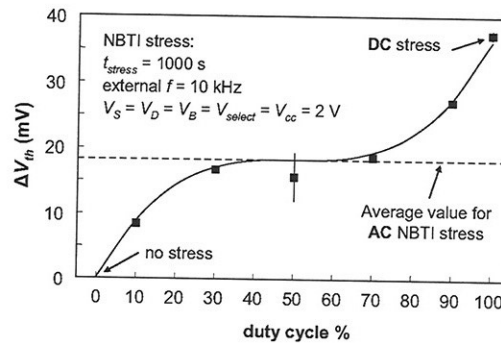


Fig. 16: ΔV_{th} resulting from AC NBTI at 10 kHz with varying duty cycle. As expected, the dependence is monotonic. The data can be described by the dependence $c \text{ (duty cycle - 50\%)}^3 + \Delta V_{th@50\%}$, with $\Delta V_{th@50\%}$ determined from Fig. 15 and c determined purely by the condition $\Delta V_{th} = 0$ V at no stress (i.e., duty cycle = 0%).

The effect of duty cycle is studied at $f = 10$ kHz using an external pulse generator (31). The result is given in Fig. 16. As expected, ΔV_{th} is monotonically increasing, with an apparent plateau around 50%. The exact shape of the duty cycle dependence remains to be confirmed, however, the reduction of 50-60% at 50% duty cycle is also consistent with earlier works (7,12).

The more realistic case of an inverter exposed to AC and DC NBTI stress is studied in Figs. 17 and 18. The shift in the maximum gain point ΔV_{inv} (Fig. 17) goes approximately as pFET $\Delta V_{th}/2$ (Fig. 15). ΔV_{inv} is again seen as frequency independent in the entire frequency range of 1 Hz – 2 GHz (Fig. 18) and again about 2x lower than the equivalent DC stress.

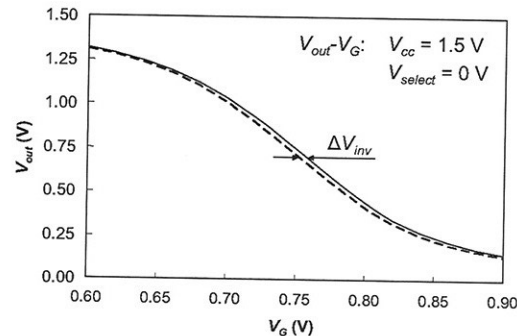


Fig. 17: The transfer curve of an inverter before and after $f = 2$ GHz NBTI stress of 1000 s. The shift ΔV_{inv} at the maximum gain point is demarcated.

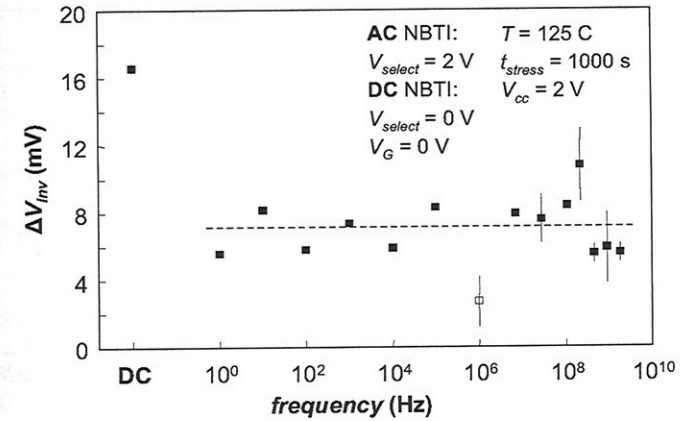


Fig. 18: The inverter maximum gain point shift ΔV_{inv} due to AC NBTI stress is seen independent of frequency in the entire frequency range of 1 Hz – 2 GHz (cf. Fig. 15). The corresponding ΔV_{inv} after DC NBTI stress obtained on identical inverters is again shown for comparison. Again, the low ΔV_{th} shift at 1 MHz (open symbol) serves as illustration of difficulties with externally-applied high frequency AC stress (see also the caption of Fig. 15).

The above results indicate that NBTI can be expected up to GHz frequencies. Furthermore, AC NBTI appears to be frequency independent up to the GHz range. The lack of any cut-off frequency further implies that there is no characteristic time scale in the NBTI mechanism down to at least 1 ns.

The results also simplify NBTI lifetime prediction. The equivalent stress time (Fig. 13) and voltage (Fig. 7) accelerations of DC and AC NBTI, combined with the measured reduction and frequency independence of AC NBTI stress (Figs. 8 and 6) allows for consistent extrapolation of AC NBTI reliability over in the entire useful frequency range 1 Hz – 2 GHz.

On-Chip Charge Pumping at GHz frequency

The issue of interface trap response time has been recently discussed with respect to trap depth profiling (34). Charge pumping at GHz frequencies has already been demonstrated on individual RF devices (35). We note that the versatile configuration of the circuit also allows using the on-chip generated AC signal for charge pumping (CP) measurements up to ~2 GHz, exceeding previous on-chip CP frequencies (36). Fig. 19a shows the typical charge pumping “hat”, with the increase in interface states due to AC NBTI clearly visible and tracking the ΔV_{th} in Fig. 19b. The lower ΔV_{th} from N_{it} is partially due to decreased CP efficiency at very high frequencies (35), accelerated recovery during CP (Fig. 4) and a possible contribution of bulk-trapped holes to ΔV_{th} (13).

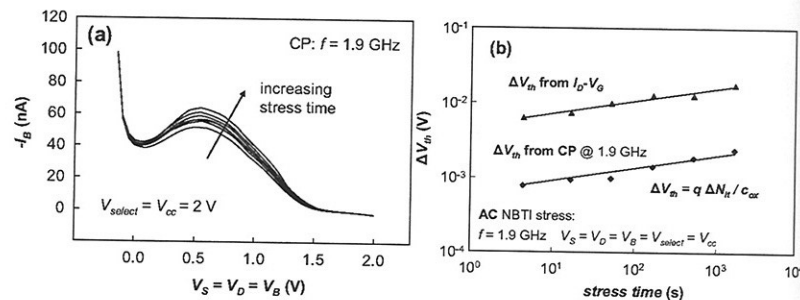


Fig. 19: (a) The substrate current during a charge pumping measurement at 1.9 GHz (fresh and at increasing stress times). $V_B = V_S = V_D$ are swept in unison (see Fig. 12a). The pFET charge pumping “hat” is visible, as is the increase in interface states ΔN_{it} after AC NBTI stress. ΔN_{it} can be evaluated as $\Delta I_B / q f W L_{eff}$, where L_{eff} is the pFET effective gate length. (b) N_{it} from a CP measurement at 1.9 GHz converted to ΔV_{th} and ΔV_{th} extracted from I_D - V_G after each stress. Both quantities follow the same trend.

Conclusions

Difficulties with evaluating Negative Bias Temperature Instability (NBTI) were discussed and shown to be linked to fast effects occurring at microsecond or possibly faster time scales. The wide distribution of time scales involved in NBTI relaxation were demonstrated and were argued to suggest participation of some sort of dispersion in the underlying NBTI mechanism. Dispersion was incorporated into the Reaction-Diffusion model through the introduction of localized deep hydrogen states. Universal behavior of the NBTI relaxation phase was demonstrated and proposed as a benchmark to distinguish among NBTI models extended with various dispersive mechanisms.

On-chip circuits were designed and fabricated for the purpose of measuring the effect of AC NBTI on individual, well-defined devices in a wide frequency range on a single wafer. The results on both single pFET's and inverters indicate that AC NBTI is independent of the frequency in the entire 1 Hz – 2 GHz range. This implies that any characteristic time scale of the NBTI mechanism must be below 1 ns. CP has been demonstrated up to the GHz range, suggesting that interface trap response time is also well below 1 ns.

References

1. D. K. Schroder and J. Babcock, *J. Appl. Phys.* **94**, 1 (2003).
2. V. Reddy, A. T. Krishnan, A. Marshall, J. Rodriguez, S. Natarajan, T. Rost, and S. Krishnan, *Proc. IRPS*, 248 (2002).
3. J. Stathis and S. Zafar, *Microelectr. Reliab.* **46**, 270 (2006).
4. M. Ershov, S. Saxena, H. Karbasi, S. Winters, S. Minehane, J. Babcock, R. Lindley, P. Clifton, M. Redford, and A. Shibkov, *Appl. Phys. Lett.* **83**, 1647 (2003).
5. G. Chen, K. Y. Chuah, M. F. Li, D. S. H. Chan, C. H. Ang, J. Z. Zheng, Y. Jin, and D. L. Kwong, *Proc. IRPS*, 196 (2003).

6. S. Rangan, N. Mielke, and E. C.C. Yeh, *Proc. IEDM*, 341 (2003).
7. T. Yang, C. Shen, M.-F. Li, C.H. Ang, C.X. Zhu, Y.-C. Yeo, G. Samudra, S.C. Rustagi, M.B. Yu, and D.-L. Kwong, *IEEE Electron Dev. Lett.* **26**, 826 (2005).
8. B. Kaczer, V. Arkhipov, R. Degraeve, N. Collaert, G. Groeseneken, and M. Goodwin, *Proc. IRPS*, 381 (2005).
9. H. Reisinger, O. Blank, W. Heinrigs, A. Mühlhoff, W. Gustin, and C. Schlünder, *Proc. IRPS*, 448 (2006).
10. M. Denais, A. Bravaix, V. Huard, C. Parthasarathy, C. Guerin, G. Ribes, F. Perrier, M. Mairy, and D. Roy, *Proc. IRPS*, 735 (2006).
11. T. Grasser, W. Göss, V. Sverdlov, and B. Kaczer, accepted to *IRPS* 2007.
12. M. A. Alam, *IEDM Tech. Digest*, 345 (2003).
13. V. Huard, M. Denais, and C. Parthasarathy, *Microelectr. Reliab.* **46**, 1 (2006).
14. B. Kaczer, V. Arkhipov, R. Degraeve, N. Collaert, G. Groeseneken, and M. Goodwin, *Appl. Phys. Lett.* **86**, 143506 (2005).
15. S. Zafar, *J. Appl. Phys.* **97**, 1 (2005).
16. M. Houssa, M. Aoulaiche, S. De Gendt, G. Groeseneken, M. M. Heyns, and A. Stesmans, *Appl. Phys. Lett.* **86**, 093506 (2005).
17. M. Houssa, M. Aoulaiche, J.L. Autran, C. Parthasarathy, N. Revil, and E. Vincent, *J. Appl. Phys.* **95**, 2786 (2004).
18. R. Fernández, B. Kaczer, A. Nackaerts, S. Demuynck, R. Rodríguez, M. Nafria, and G. Groeseneken, *Proc. IEDM Tech. Digest*, 337 (2006).
19. A. T. Krishnan, V. Reddy, S. Chakravarthi, J. Rodriguez, S. John, and S. Krishnan, *IEDM Tech. Dig.*, 349 (2003).
20. Denais, A. Bravaix, V. Huard, C. Parthasarathy, G. Ribes, F. Perrier, Y. Rey-Tauriac, and N. Revil, *IEDM Tech. Digest*, 109 (2004).
21. Y. Mitani, H. Satake, and A. Toriumi, *Proc. ECS Int. Symp. “Silicon Nitride, Silicon Dioxide Thin Films, and Other Emerging Dielectrics VIII”*, 340 (2005).
22. C. Shen, M.-F. Li, C. E. Foo, T. Yang, D. M. Huang, A. Yap, G. S. Samudra, Y.-C. Yeo, *IEDM Tech. Digest*, 333 (2006).
23. L. Tsetseris, X. J. Zhou, D. M. Fleetwood, D. R. Schrimpf, and S. T. Pantelides, *Appl. Phys. Lett.* **86**, 142103 (2005).
24. A. Stesmans, *Appl. Phys. Lett.* **68**, 2076 (1996).
25. T. Grasser, W. Göss, and B. Kaczer, *Proc. IIRW*, 5 (2006).
26. D. Varghese, D. Saha, S. Mahapatra, K. Ahmed, F. Nouri, and M. Alam, *IEDM Tech. Dig.*, 701 (2005).
27. B. Kaczer, V. Arkhipov, M. Jurczak, G. and Groeseneken, *Microelectr. Reliab.* **80**, 122 (2005).
28. S. Chakravarthi, A.T. Krishnan, V. Reddy, C.F. Machala, and S. Krishnan, *Proc. IRPS*, 273 (2004).
29. K. O. Jeppsson and C. M. Svensson, *J. Appl. Phys.* **48**, 2004 (1977).
30. B. Zhu, J. S. Suehle, Y. Chen, and J. B. Bernstein, *Proc. IRW*, 125 (2002).
31. W. Abadeer and W. Ellis, *Proc. IRPS*, 17 (2003).
32. T. Nigam and E. B. Harris, *Proc. IRPS*, 289 (2006).
33. B. Kaczer, R. Degraeve, G. Groeseneken, M. Rasras, S. Kubicek, E. Vandamme, and G. Badenes, *IEDM Tech. Digest*, 553 (2000).
34. Y. Wang, V. Lee, K. P. Cheung, *IEDM Tech. Digest*, 763 (2006).
35. G. T. Sasse and J. Schmitz, *Proc. IRPS*, 627 (2006).
36. H.-H. Ji et al., *IEDM Tech. Digest*, 721 (2005).